



## NRC Publications Archive Archives des publications du CNRC

### **A comparison between CloudSat and aircraft data for a multilayer, mixed phase cloud system during the Canadian CloudSat-CALIPSO Validation Project**

Barker, H. W.; Korolev, A. V.; Hudak, D. R.; Strapp, J. W.; Strawbridge, K. B.; Wolde, M.

This publication could be one of several versions: author's original, accepted manuscript or the publisher's version. / La version de cette publication peut être l'une des suivantes : la version prépublication de l'auteur, la version acceptée du manuscrit ou la version de l'éditeur.

For the publisher's version, please access the DOI link below. / Pour consulter la version de l'éditeur, utilisez le lien DOI ci-dessous.

#### **Publisher's version / Version de l'éditeur:**

<https://doi.org/10.1029/2008JD009971>

*Journal of Geophysical Research*, 113, 2008-12-06

#### **NRC Publications Record / Notice d'Archives des publications de CNRC:**

<https://nrc-publications.canada.ca/eng/view/object/?id=39063e51-5b2a-4af5-8ed0-1ce78c1531ae>

<https://publications-cnrc.canada.ca/fra/voir/objet/?id=39063e51-5b2a-4af5-8ed0-1ce78c1531ae>

Access and use of this website and the material on it are subject to the Terms and Conditions set forth at

<https://nrc-publications.canada.ca/eng/copyright>

READ THESE TERMS AND CONDITIONS CAREFULLY BEFORE USING THIS WEBSITE.

L'accès à ce site Web et l'utilisation de son contenu sont assujettis aux conditions présentées dans le site

<https://publications-cnrc.canada.ca/fra/droits>

LISEZ CES CONDITIONS ATTENTIVEMENT AVANT D'UTILISER CE SITE WEB.

**Questions?** Contact the NRC Publications Archive team at

PublicationsArchive-ArchivesPublications@nrc-cnrc.gc.ca. If you wish to email the authors directly, please see the first page of the publication for their contact information.

**Vous avez des questions?** Nous pouvons vous aider. Pour communiquer directement avec un auteur, consultez la première page de la revue dans laquelle son article a été publié afin de trouver ses coordonnées. Si vous n'arrivez pas à les repérer, communiquez avec nous à PublicationsArchive-ArchivesPublications@nrc-cnrc.gc.ca.



# A comparison between CloudSat and aircraft data for a multilayer, mixed phase cloud system during the Canadian CloudSat-CALIPSO Validation Project

H. W. Barker,<sup>1</sup> A. V. Korolev,<sup>1</sup> D. R. Hudak,<sup>1</sup> J. W. Strapp,<sup>1</sup> K. B. Strawbridge,<sup>2</sup> and M. Wolde<sup>3</sup>

Received 15 February 2008; revised 14 May 2008; accepted 2 September 2008; published 6 December 2008.

[1] Reflectivities recorded by the W-band Cloud Profiling Radar (CPR) aboard NASA's CloudSat satellite and some of CloudSat's retrieval products are compared to Ka-band radar reflectivities and in situ cloud properties gathered by instrumentation on the NRC's Convair-580 aircraft. On 20 February 2007, the Convair flew several transects along a 60 nautical mile stretch of CloudSat's afternoon ground track over southern Quebec. On one of the transects it was well within CloudSat's radar's footprint while in situ sampling a mixed phase boundary layer cloud. A cirrus cloud was also sampled before and after overpass. Air temperature and humidity profiles from ECMWF reanalyses, as employed in CloudSat's retrieval stream, agree very well with those measured by the Convair. The boundary layer cloud was clearly visible, to the eye and lidar, and dominated the region's solar radiation budget. It was, however, often below or near the Ka-band's distance-dependent minimum detectable signal. In situ samples at overpass revealed it to be composed primarily of small, supercooled droplets at the south end and increasingly intermixed with ice northward. Convair and CloudSat CPR reflectivities for the low cloud agree well, but while CloudSat properly ascribed it as overcast, mixed phase, and mostly liquid near the south end, its estimates of liquid water content LWC (and visible extinction coefficient  $\kappa$ ) and droplet effective radii are too small and large, respectively. The cirrus consisted largely of irregular crystals with typical effective radii  $\sim 150 \mu\text{m}$ . While both CPR reflectivities agree nicely, CloudSat's estimates of crystal number concentrations are too large by a factor of 5. Nevertheless, distributions of ice water content and  $\kappa$  deduced from in situ data agree quite well with values retrieved from CloudSat algorithms.

**Citation:** Barker, H. W., A. V. Korolev, D. R. Hudak, J. W. Strapp, K. B. Strawbridge, and M. Wolde (2008), A comparison between CloudSat and aircraft data for a multilayer, mixed phase cloud system during the Canadian CloudSat-CALIPSO Validation Project, *J. Geophys. Res.*, 113, D00A16, doi:10.1029/2008JD009971.

## 1. Introduction

[2] It is well known that numerical simulations of global and regional climate can be impacted significantly when seemingly small, but systematic, changes are made to the radiative properties of model clouds [e.g., *Slingo and Slingo*, 1991]. While progress has been made recently on aspects of modeling radiative transfer for cloudy atmospheres in global climate models (GCMs) [*Barker et al.*, 2008], there remains much uncertainty regarding representation of cloud characteristics in GCMs. This uncertainty

rests, in part, on the fact that GCM clouds have to be assessed globally which necessitates use of satellite measurements. Passive sensors aboard operational and research satellites are relatively inexpensive, but only vertically integrated and effective cloud properties are inferable from their data. In order for advancement to occur, information pertaining to vertical and horizontal codistributions of cloud properties is required.

[3] In response to this requirement, NASA, with contributions from the Canadian Space Agency (CSA), launched the CloudSat satellite, with its 94-GHz (W-band) cloud-profiling radar (CPR), on 29 April 2006 into a 700 km high, Sun-synchronous, near-polar orbit [*Stephens et al.*, 2002]. Building on the success of ground- and aircraft-based CPRs that revolutionized many cloud physics programmes [e.g., *Stevens et al.*, 2005; *Illingworth et al.*, 2007; *Verlinde et al.*, 2007], CloudSat's CPR is providing the first global view of the vertical and horizontal structure of cloud and precipitation. As with the ground and aircraft programmes, CloudSat's

<sup>1</sup>Cloud Physics and Severe Weather Research Section, Environment Canada, Toronto, Ontario, Canada.

<sup>2</sup>Centre for Atmospheric Research Experiments, Environment Canada, Egbert, Ontario, Canada.

<sup>3</sup>Institute for Aerospace Research, National Research Council of Canada, Ottawa, Ontario, Canada.

data will synergize ultimately with data from sensors on other A-train satellites with whom it flies in tight formation: Aqua and PARASOL with their passive sensors; CALIPSO with its dual-wavelength, three channel lidar; and, the as yet unlaunched, OCO with its passive spectrometers.

[4] Being the first CPR in space, it is imperative that cloud properties inferred from CloudSat's measurements be assessed rigorously; because of their novelty, and also because it is well known that inference of cloud properties from W-band CPR data are still rife with uncertainty [e.g., *Fox and Illingworth, 1997; Sekelsky et al., 1999; L'Ecuyer and Stephens, 2002*]. The most obvious, though far from straightforward, method of assessing CloudSat products is to underfly CloudSat, and by default the entire A-train, with (an) aircraft that (is) are capable of both remotely sensing clouds with instruments resembling those in the A-train and making in situ observations of clouds within CloudSat's field of view. Flights such as these defined the essence of the Canadian CloudSat-CALIPSO Validation Project (C3VP) which took place over Southern Ontario and Quebec between 11/2006 and 3/2007 [see *Hudak et al., 2006*]. C3VP's goal is to assess the performance of CloudSat and its retrieval algorithms, and to a lesser extent CALIPSO, for cold weather cloud and precipitation systems. This report documents a comparison between C3VP and CloudSat data for one overpass flight that involved a multilayer, mixed phase cloud ensemble.

[5] Section 2 contains a succinct summary of CloudSat and its retrieval algorithm. Section 3 provides a summary of C3VP and some of the aircraft-mounted instrumentation. Section 4 presents results from the flight on 20 February 2007. Conclusions are drawn in section 5.

## 2. CloudSat

### 2.1. Background

[6] The A-train satellite constellation's sequence of orbits repeats every 233 orbits, or 16 days [*Stephens et al., 2002*]. The ultimate intention is to synergize A-train data and thus produce profiles of estimated cloud characteristics that have hitherto been restricted to fixed surface, and occasional aircraft, measurements. The most relevant data will come, respectively, from CloudSat's and CALIPSO's near-nadir-pointing CPR and dual-channel lidars, narrowband and broadband radiances from Aqua's MODIS and CERES instruments, and supplementary data from the European Centre for Medium-Range Weather Forecasts (ECMWF) model analyses.

[7] The beam width of CloudSat's CPR is  $\sim 1.4$  km. With 37,081 radar profiles per orbit, each profile corresponds to a horizontal distance of  $\sim 1.1$  km. Hence, there is some overlap along track. Vertical resolution of its range gates is  $\sim 480$  m; but oversampling halves it to  $\sim 240$  m [*Stephens et al., 2002*]. Minimum detectable signal of CloudSat's CPR is approximately  $-31$  dBZ. Standard data products include both macrophysical and microphysical cloud properties. Macrophysical properties include cloud occurrence, cloud base and cloud top altitudes, cloud thickness, and precipitation occurrence. While these features can be derived directly from CloudSat's *CPR\_Cloud\_mask* field, synergy with CALIPSO's lidar data can be crucial [e.g., *Barker, 2008*]. Microphysical properties include vertical profiles of

cloud liquid and ice water contents, effective particle sizes, and particle concentrations. The highest-level derived properties are broadband radiative flux profiles.

### 2.2. CloudSat Retrieval Process

[8] *Austin [2007]* discusses CloudSat's retrieval process in greater detail than in this précised version. The process begins by assuming that cloud droplets of radius  $r$  are distributed as

$$N(r) = \frac{N_T}{\sqrt{2\pi}\sigma_{\log}r} \exp\left[\frac{-\ln^2\left(\frac{r}{r_g}\right)}{2\sigma_{\log}^2}\right] \quad (1)$$

where

$$\begin{aligned} r_g &= e^{\overline{\ln r}}, \\ \sigma_{\log} &= \overline{\ln \sigma_g}, \\ \sigma_g^2 &= (\overline{\ln r} - \overline{\ln r_g})^2, \end{aligned}$$

and where  $N_T$  is droplet number concentration,  $r_g$  is geometric mean radius,  $\sigma_{\log}$  is distribution width parameter, and  $\sigma_g$  is geometric standard deviation. The same distribution is assumed for ice crystals except  $r$  is replaced by diameter  $D$  of an equivalent mass ice sphere. After a series of simplifying assumptions, profiles of these parameters are solved for via optimal estimation by iteratively minimizing a cost function, in conjunction with their a priori estimates and error covariances, constrained by the measured radar reflectivity profile. The solutions are then integrated to give cloud water contents defined as

$$CWC = \begin{cases} \frac{4\pi}{3} \rho_{\text{liq}} \int_0^\infty r^3 N(r) dr = \frac{4\pi}{3} \rho_{\text{liq}} N_T r_g^3 \exp\left(\frac{9}{2}\sigma_{\log}^2\right) 10^{-3} & ; \text{liquid water content (LWC)} \\ \frac{\pi}{6} \rho_{\text{ice}} \int_0^\infty D^3 N(D) dD = \frac{\pi}{6} \rho_{\text{ice}} N_T D_g^3 \exp\left(\frac{9}{2}\sigma_{\log}^2\right) 10^{-3} & ; \text{ice water content (IWC),} \end{cases} \quad (2)$$

and particle effective sizes defined as

$$r_e = \begin{cases} \frac{\int_0^\infty r^3 N(r) dr}{\int_0^\infty r^2 N(r) dr} = r_g \exp\left(\frac{5}{2}\sigma_{\log}^2\right) & ; \text{droplets} \\ \frac{1}{2} \frac{\int_0^\infty D^3 N(D) dD}{\int_0^\infty D^2 N(D) dD} = \frac{1}{2} D_g \exp\left(\frac{5}{2}\sigma_{\log}^2\right) & ; \text{crystals,} \end{cases} \quad (3)$$

where  $\rho_{\text{liq}}$  and  $\rho_{\text{ice}}$  are liquid and ice densities. CloudSat assesses cloud phase from ECMWF estimates of temperature  $T$ . When  $T > 0^\circ\text{C}$  it is very likely that ice is absent, and when  $T \lesssim -20^\circ\text{C}$  it is very likely that liquid droplets are either not present or they are so few in number as to be unimportant. But between these limits both ice and liquid can, and often do, coexist; and because their scattering properties and size distributions differ markedly, this poses a problem for CloudSat retrievals. Currently, retrievals proceed as follows (see *Austin [2007]* for details). If the temperature of a cell in a column falls between the above mentioned values, two retrievals are performed: one assumes the column is entirely liquid, the other entirely ice. Where  $T < -20^\circ\text{C}$ , it is assumed that radar reflectivity arose from crystals alone; where  $T > 0^\circ\text{C}$ , it is assumed that

only droplets were present. Size distributions and water contents are then solved for as mentioned earlier. For cells with  $-20^\circ < T < 0^\circ$ , the ice and liquid solutions are scaled linearly with  $T$  by adjusting their respective values of  $N_7$  while maintaining measured radar reflectivity.

### 3. Canadian CloudSat-CALIPSO Validation Project

#### 3.1. Background

[9] As mentioned in the Introduction, the primary goal of C3VP is to assess the performance of CloudSat and its retrieval algorithms for cold weather cloud and precipitation systems. C3VP consisted of instrumentation at a fixed ground site and on the National Research Council's (NRC's) Convair-580 aircraft. The current study deals exclusively with aircraft data (see *Hudak et al.* [2006] for details on the ground site). The aircraft portion of C3VP had two objectives: make remote sensing measurements to help verify CloudSat's CPR, and make in situ measurements of cloud properties to help verify CloudSat retrievals. The first C3VP flight was on 31 October 2006 and the last was on 27 February 2007. Guided by the A-train's 16-day period, C3VP consisted of four intensive observing periods (IOPs). Each IOP lasted  $\sim 12$  days and typically saw 6 flights (see <http://c3vp.org/> for details). There was a total of 21 research flights with most lasting  $\sim 4.5$  h for a total of 95 h of flying time. Generally, five flights per IOP were devoted to sun-up overpasses, which occurred between  $\sim 1300$  and  $\sim 1340$  local time depending on ground track position in the time zone, while one was reserved for a night overpass, which occurred at  $\sim 0230$  local time. A relatively small number of hours were reserved for "flights of opportunity" that targeted clear-sky conditions for lidar aerosol studies and precipitation events outside overpass times.

[10] Roughly 6 h before an overpass, a 60 nautical mile target segment of CloudSat's ground track was identified for the Convair to focus data collection along. The Convair was almost always near the center of the target segment at overpass. In fact, the Convair itself often appears in CloudSat data; and while its up-facing W-band radar was turned off at overpass, ground surface reflection of its down-facing W-band was captured in CloudSat data in the form of a column of interference. These fleeting interruptions semaphored that the Convair was well within CloudSat's radar beam. As C3VP was the inaugural experiment for the Convair's W-band, its data were still being processed at the time of writing and thus not used here. Once overpass occurred, several additional transects were flown at various altitudes along the target segment. They often included a rapid and shallow sinusoidal flight line (referred to as "porpoising") as well as tight spirals that tried to maximize vertical in situ sampling of cloud. When measurements were being taken, the Convair's airspeed was  $\sim 100$  m s $^{-1}$ . Hence, 60 nautical mile segments were covered in  $\sim 17$  min.

#### 3.2. Aircraft Instrumentation

[11] A variety of microphysical and remote sensing instruments on the Convair-580 were brought to bear on the assessment of CloudSat data and retrieval products. These subsections provide brief descriptions of the most relevant instruments.

##### 3.2.1. Lidar

[12] AERIAL (Aerosol Imaging Airborne Lidar) was modified from the configuration used previously [*Strawbridge and Snyder*, 2004] to provide measurements similar to those obtained by CALIPSO. The new design employed Continuum InliteIII (30 Hz) lasers that emit simultaneously at 1064 nm and 532 nm wavelengths. For eye safety, both beams were diverged to 5 mrad before being transmitted into the atmosphere. AERIAL provided simultaneous upward/downward, 1 s averaged, vertical profiles at a sampling rate of 50 MHz ( $\sim 3$  m vertical resolution).

##### 3.2.2. Cloud Profiling Ka-Band Radar

[13] The Convair-580 is equipped with a 34.66-GHz Ka-band radar (neither Dopplerized nor polarimetric) with fixed up- and down-pointing 30.6 cm diameter antennae mounted in the aircraft wing roots. It is a US military surplus AN-APD-7 radar adapted for research and flight guidance purposes. The radar system has a vertical resolution of 25 m, a beam width of  $2^\circ$ ; and a sensitivity of approximately  $-29$  dBZ at 1 km. Further specifications and data examples are given by *Jordan et al.* [2000]. The radar was calibrated before the project started and immediately after it ended. The lens of the down-pointing antenna cracked, and was replaced, in late January 2008, so the end-of-project calibration was applied to all flights after the antenna was replaced. The radar is estimated to be accurate to within  $\pm 2$  dB.

##### 3.2.3. Cloud Particles

[14] Concentrations and sizes of cloud droplets were measured by two Particle Measuring Systems (PMS) forward scattering spectrometer probes (FSSP-100) [*Knollenberg*, 1981]. The probes were configured so as to count droplets in one of fifteen size bins in the nominal diameter range of 2.5–47.5  $\mu\text{m}$ . Regular maintenance and calibration of the FSSP probes were carried out in order to minimize potential errors in droplet sizing. Dead time losses and coincidence errors were taken into account during data processing [*Baumgardner et al.*, 1985].

[15] Large cloud particles were measured by the 2-D imaging optical array probes (OAP) PMS OAP-2DC and OAP-2DP which operated in the nominal size ranges of 25–800  $\mu\text{m}$  and 200–6400  $\mu\text{m}$  with 25  $\mu\text{m}$  and 200  $\mu\text{m}$  pixel resolution, respectively [*Knollenberg*, 1981]. These instruments provided shadow binary images and concentrations of hydrometeors. Sizes of incomplete images, partially captured in the probes' fields of view, were reconstructed following *Korolev and Sussman* [2000]. Data from these probes were averaged over 4 s intervals in order to provide statistically significant numbers of images for estimation of particle concentration and habit recognition analyses. Habit recognition analysis was conducted on the basis of *Korolev and Sussman's* [2000] algorithm. Ice particle habits were segregated into: spheres; needles/columns; dendrites; and irregulars. OAP data were used to identify ice and liquid clouds via particle image recognition and particle size distribution calculations.

##### 3.2.4. Cloud Water Contents

[16] Cloud liquid water content (LWC) was measured by a King hot-wire probe [*King et al.*, 1978]. The estimated accuracy of this probe is no worse than 10%. Cloud Total Water Content (TWC; ice + liquid) was estimated using the Nevzorov probe [*Korolev et al.*, 1998]. After a series of wind tunnel tests using high-speed video, the Nevzorov

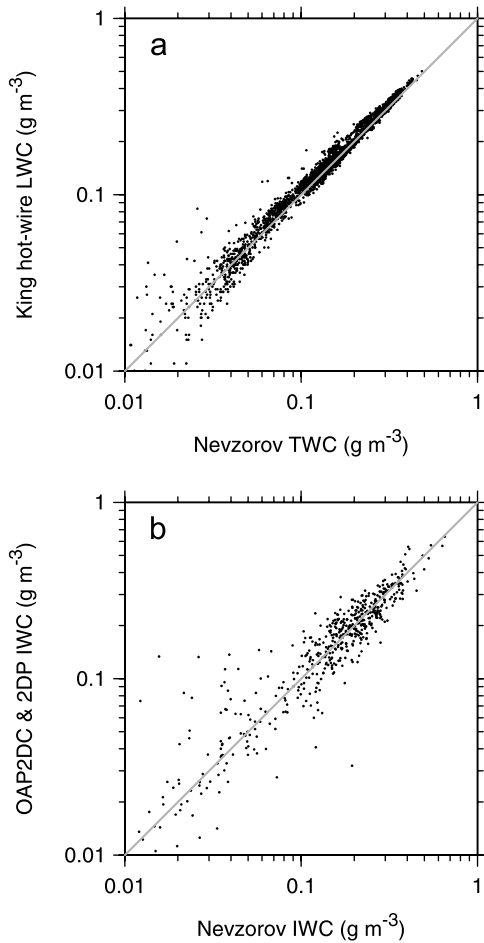


**Figure 1.** (a) Total cloud water content measured by the King hot-wire probe when liquid phase was dominant plotted against corresponding values from the Nevzorov total water probe. These data were obtained on the 20 February flight. (b) Ice water content estimated from OAP 2DC and 2DP imagery plotted against values from the Nevzorov ice water content probe. These data were obtained on a flight made on 25 February 2007 and span a much wider range than those on the 20 February flight. All instruments were mounted on the Convair's wings.

TWC sensor was modified by deepening the conical intake [Korolev *et al.*, 2008]. The purpose of this modification was to reduce the likelihood of ice particles bouncing out of the cone; an effect that leads to underestimation of cloud ice water content (IWC). Comparisons to IWC measured by the CVI probe (DMT Inc. [Twohy *et al.*, 1997]), conducted in ice clouds, showed good agreement between these two instruments for IWC values  $\lesssim 1 \text{ g m}^{-3}$ .

[17] In mixed phase clouds IWC and LWC were deduced from measurements made by the Nevzorov and King probes following the procedure described by Korolev *et al.* [2003]. This accounts for residual effects of ice on the King probe.

### 3.2.5. Extinction Coefficient

[18] Monochromatic extinction coefficient for spherical droplets at wavelength  $\lambda$  is defined as

$$\kappa_{\lambda} = \int_0^{\infty} \pi r^2 Q_{\text{ext}}(r; \lambda) N(r) dr \quad (4)$$

where  $r$  is radius,  $N(r)$  is droplet size distribution, and  $Q_{\text{ext}}$  is extinction efficiency. Thus, after traversing distance  $Z$ , the intensity of a column of light of initial intensity  $I_{\lambda}^*$  would be

$$I_{\lambda} = I_{\lambda}^* e^{-\int_0^Z \kappa_{\lambda}(z) dz}. \quad (5)$$

Mean extinction coefficient across  $Z$  is then defined, and computed, as

$$\kappa_{\lambda} = \frac{\ln\left(\frac{I_{\lambda}^*}{I_{\lambda}}\right)}{Z}. \quad (6)$$

Cloud extinction coefficient was inferred from data gathered by a newly developed Extinction Probe. This probe's principle of operation is based on attenuation of a known source of light traversing a known distance to a receiver. The Extinction Probe consists of an optical unit that combines a transmitter and receiver as well as a retro-reflector. A column of light  $I_{\lambda}^*$  is generated by an LED ( $\lambda = 0.635 \text{ } \mu\text{m}$ ), travels 2.5 m to the retroreflector, and then travels the same distance back (i.e.,  $Z = 5 \text{ m}$ ) to the optical unit where it is measured  $I_{\lambda}$  by a photodetector, and (6) is then used to estimate  $\kappa_{\lambda}$ . The sensitivity of this device is such that  $\kappa_{\lambda}$  can be estimated in the range  $[0.2, 200] \text{ km}^{-1}$ . Note that while (4) assumes spherical particles,  $\kappa_{\lambda}$  can be solved for via (6) for any particle.

### 3.2.6. Quality Control of Convair Data

[19] Microphysical parameters measured by different probes are always cross checked for consistency with other relevant instruments. This serves to reveal and isolate improperly functioning instruments. It also fosters confidence that in situ data used to assess data collected, or inferred, from other sources, such as CloudSat, are reliable.

[20] Figure 1a shows LWC measured by the King hot-wire plotted against coincidental values from the Nevzorov TWC probe. The systematic difference in LWC values of  $\sim 5\%$  can be explained by differences in collection efficiencies due to different geometrical dimensions of their intakes [Korolev *et al.*, 1998].

[21] IWC can be estimated from OAP 2-D imagery through the size-to-mass relationship  $M = aD^b$ , where  $M$  is mass,  $D$  is diameter of an ice particle,  $a = 7.38 \times 10^{-11}$ , and  $b = 1.9$  [Brown and Francis, 1995]. Figure 1b shows a comparison of IWC, in ice cloud, measured by the Nevzorov TWC sensor and that computed from OAP-2DC and 2DP imagery. This latter method of estimation was used when  $\text{IWC} > 0.01 \text{ g m}^{-3}$ ; which is when the Nevzorov TWC probe's accuracy degrades.

[22] For liquid clouds,  $\kappa$  can be approximated via discretization of (4) and application of Mie theory [Wiscombe, 1980] to droplet size distributions measured by FSSP as

$$\kappa_{\text{FSSP}} = \pi \sum_{j=1}^{15} Q_{\text{ext}}(r_j) n_j r_j^2 \quad (7)$$

where  $n_j$  and  $r_j$  are droplet concentration and mean radius in the  $j$ th bin. Figure 2a shows  $\kappa$  measured directly by the Extinction Probe  $\kappa_{\text{EP}}$  compared to  $\kappa_{\text{FSSP}}$  computed from droplet size spectra measured at the same time by FSSP.

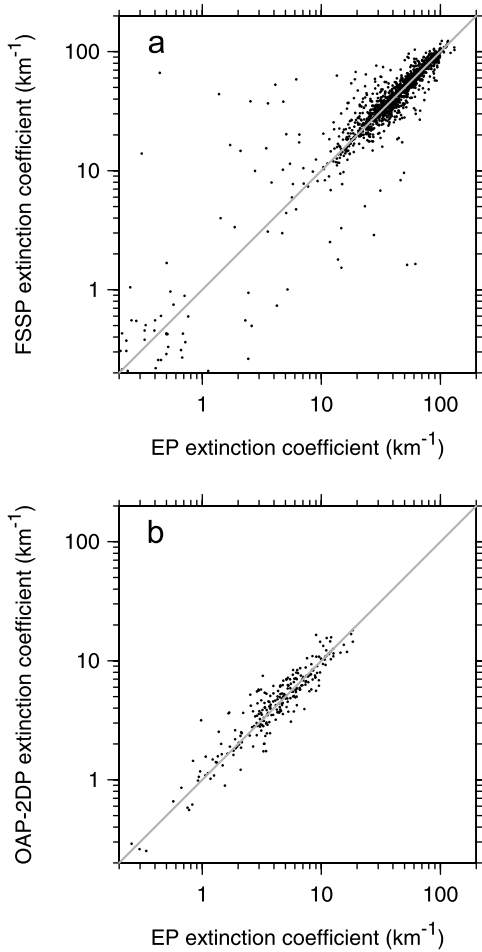


**Figure 2.** (a) Liquid phase cloud extinction coefficient computed on the basis of droplet number concentrations measured by an FSSP probe that counts droplets with diameters between 2.5 and 47.5  $\mu\text{m}$  plotted against corresponding values measured directly by the extinction probe. These data were obtained on the 20 February flight. (b) Ice cloud extinction coefficient computed on the basis of OAP 2DP imagery plotted against values measured directly by the extinction probe. These data, obtained on a flight made on 25 February 2007, spanned a much wider range than those on the 20 February flight. All instruments were mounted on the Convair's wings.

Despite measurement errors inherent to FSSP probes, this intercomparison of extinction coefficients is very good.

[23] Extinction coefficient associated with ice particles  $\kappa_{\text{ice}}$  can be approximated by integrating particle shadow areas in OAP-2DC and 2DP imagery as

$$\kappa_{\text{OAP}} = \frac{2}{Su\Delta t} \sum_j A_j \quad (8)$$

where  $A_j$  is shadow area of the  $j$ th cloud particle,  $S$  is sample area,  $u$  is true air speed,  $\Delta t$  is averaging time interval, and assuming that  $Q_{\text{ext}} \approx 2$ . Figure 2b shows a comparison between  $\kappa_{\text{EP}}$  and  $\kappa_{\text{OAP}}$  for pure ice clouds. By most standards this level of agreement is very satisfactory.

[24] Assume now that for mixed phase cloud:  $\kappa_{\text{ice}} \approx \kappa_{\text{OAP}}$ ; OAP-2DC and 2DP are insensitive to cloud droplets with  $D < 30 \mu\text{m}$ ; and that there are no large droplets associated with drizzle and rain (often the case for clouds sampled during C3VP). Therefore, since total  $\kappa \approx \kappa_{\text{EP}}$  is the sum of constituent extinction coefficients, extinction coefficient for droplets  $\kappa_{\text{liq}}$  can be estimated as

$$\begin{aligned} \kappa_{\text{liq}} &= \kappa - \kappa_{\text{ice}} \\ &\approx \kappa_{\text{EP}} - \kappa_{\text{OAP}} \end{aligned} \quad (9)$$

which should agree well with  $\kappa_{\text{FSSP}}$ . As seen later, for the flight considered here, when mixed phase conditions occurred  $\kappa_{\text{FSSP}} \gg \kappa_{\text{OAP}}$ . Thus, since it was just shown that  $\kappa_{\text{EP}} \approx \kappa_{\text{FSSP}}$ , the agreement between  $\kappa_{\text{liq}}$  from (9) and  $\kappa_{\text{FSSP}}$  will resemble that seen in Figure 2b.

#### 4. Results

[25] The flight considered here, C3VP flight 18, occurred on 20 February 2007. During the flight, and at overpass, two distinct cloud layers were present: a cirrus cloud that consisted entirely of ice crystals; and a mixed phase boundary layer cloud whose precipitation was reaching the ground. Figure 3 shows the MODIS 12  $\mu\text{m}$  image made either side of the Convair-CloudSat alignment. The red circle shows the 60 nautical mile diameter region that contained the target segment of CloudSat's ground track. It indicates a significant amount of cirrus cloud streaming from west to east across the target area (white), a blanket of low cloud over most of the region (light grey), and a cloudless patch NW of the target areas (dark grey). Figure 4a shows the location of the Convair's flight path along the ground track as well as the 60 nautical mile circle shown in Figure 3. Figure 4b shows time series of Convair longitude and altitude.

[26] Figure 5 shows profiles of air temperature and specific humidity measured by the Convair and as reported by CloudSat on the basis of ECMWF analyses. Generally

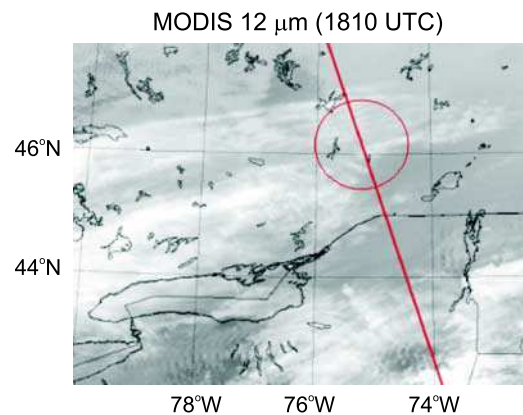


**Figure 3.** The 12  $\mu\text{m}$  thermal image obtained by the Moderate Resolution Imaging Spectroradiometer (MODIS) at 1810 UTC on 20 February 2007. Red diagonal line shows CloudSat's ground track while the red circle centered on it indicates the C3VP 60 nautical mile target segment in which the Convair maneuvered and took measurements.

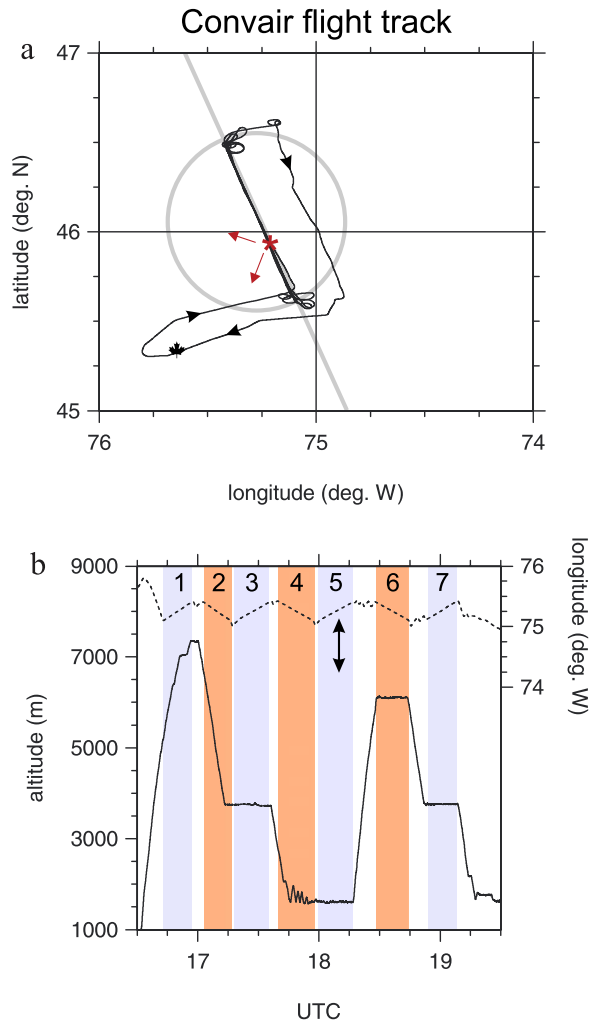


**Figure 4.** (a) Convair’s ground track on 20 February 2007. It left Ottawa, indicated by the maple leaf, at 1630 UTC and returned at 1952 UTC. CloudSat overpass occurred at 1810 UTC just north of the center of the circle. Asterisk marks the location of the Convair at the time the photographs shown in Figure 7 were taken while arrows show the camera directions. (b) Convair altitude (solid line) and longitude (dashed line). Blue and red enumerated vertical columns demarcate legs along CloudSat’s ground track. Those in blue correspond to northbound legs, and those in red correspond to southbound legs. The arrow in leg 5 indicates CloudSat overpass.

speaking, these two sets of data agree extremely well; even down to the temperature inversion near 1.5 km in altitude. [27] The remainder of this section describes radar reflectivity and cloud characteristics experienced by the Convair during this flight, and compares Convair in situ observations to observations and inferences from CloudSat. Radar reflectivities are discussed first. Given that the cloud layers were so distinct, each is discussed separately.

**4.1. Radar Reflectivities**

[28] As will be seen in subsequent subsections, the vast majority of cloud particles measured on this flight were

smaller than 1 mm. As such, both the W- and Ka-band radar beams experienced predominantly Rayleigh scattering, and so their reflectivities should be in close agreement.

[29] Figure 6 shows Convair Ka-band reflectivities and lidar backscatter ratios relative to clear sky for the northbound leg 3. Figure 7 shows two photographs taken in the midst of this leg at 1724 UTC. The radar and lidar images show two well-defined cloud layers. The upper cloud, which was streaming rapidly from west to east, was obviously ice and of low optical density as the lidar had no problem profiling it. Moreover, the radar had little problem detecting most of it too. On the other hand, the lidar beam was completely attenuated in the upper reaches of the low cloud while the radar beam was transmitted easily to the

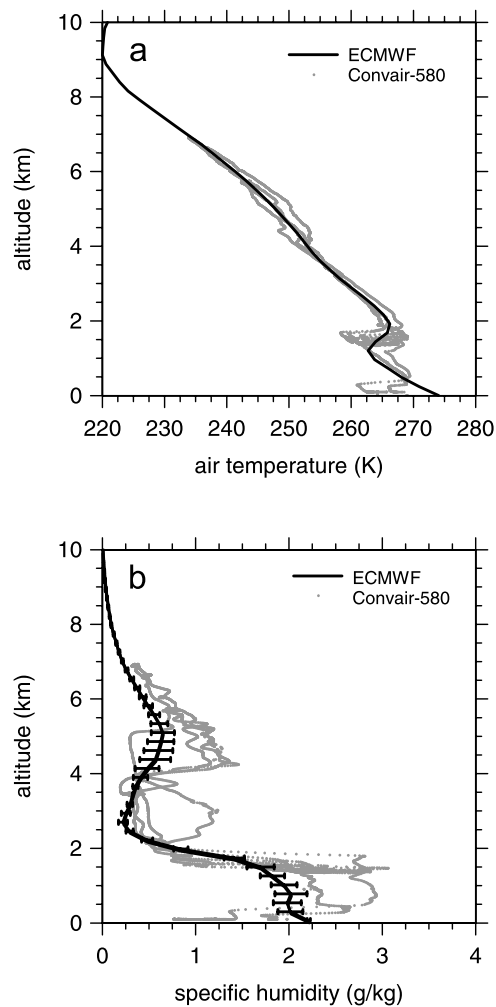


**Figure 5.** Mean values along the 60 nautical mile target segments shown in Figures 3 and 4 of air temperature and specific humidity, as supplied by ECMWF and available from CloudSat data files, as functions of altitude. Horizontal error bars indicate standard deviation of specific humidity. Air temperature along the segment was almost constant. Dots are 1 s values measured on the Convair. Calculations of saturation specific humidity using Convair data indicate a saturated layer from ~1.4 to ~1.9 km and another from ~4 km to above the Convair’s highest point.

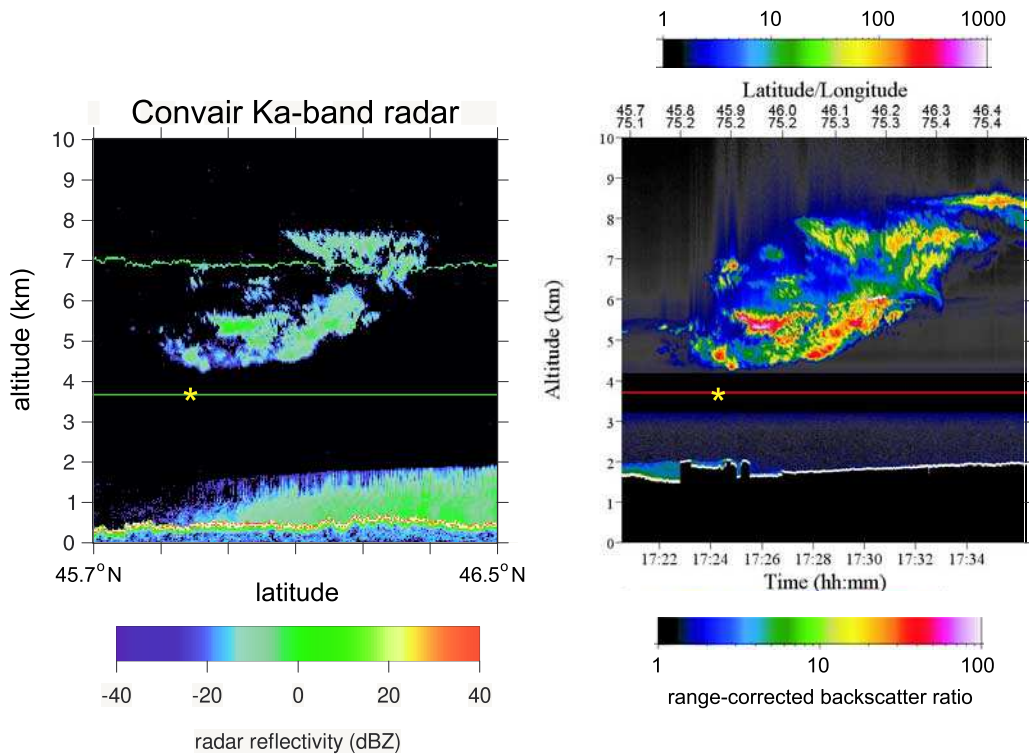


**Figure 6.** Reflectivity cross section measured by the Ka-band CPR on the Convair during the 3.8 km level flight of leg 3 (see Figure 4b) along with coincidental 1064 nm lidar backscatter (defined as the ratio between measured reflectance to that expected for clear sky). The straight horizontal green line indicates Convair altitude, and the jagged green line is the result of surface reflection (imperfect switching of antennae). Note that the scale for the down-facing lidar runs from 1 to 100 while for the up-facing lidar it runs from 1 to 1000.

surface. Indeed, at the south end of the leg, radar reflectivities were below the detection limit of the Ka-band radar. The photographs corroborate lidar data by showing that the lower cloud was dense, extensive, and dominated the solar radiation budget despite being almost invisible to the radar.

[30] On the basis of observations during leg 3 and having already sampled the upper cloud on legs 1 and 2, it was decided to sample the upper portion of the lower cloud during overpass which occurred on northbound leg 5 at

1810:40 UTC. Figure 8 shows CloudSat reflectivities along with Convair reflectivities at its native 25 m vertical and ~100 m horizontal resolutions as well as the Convair’s reflectivities degraded to CloudSat’s resolution. Despite the 250 m radar dead zone above and below the Convair and the column of interference in CloudSat data generated by ground reflection of the Convair’s down-facing W-band radar, the agreement between satellite and aircraft radars is striking from a visual perspective; from the slow, northward rise of the low cloud’s top to the form and magnitude of



**Figure 7.** Photographs made from the Convair at 1724 UTC (~45 min before overpass) (see Figure 4) looking in various directions as indicated. The point at which the photographs were taken is marked by the asterisk on both cross sections shown in Figure 6.

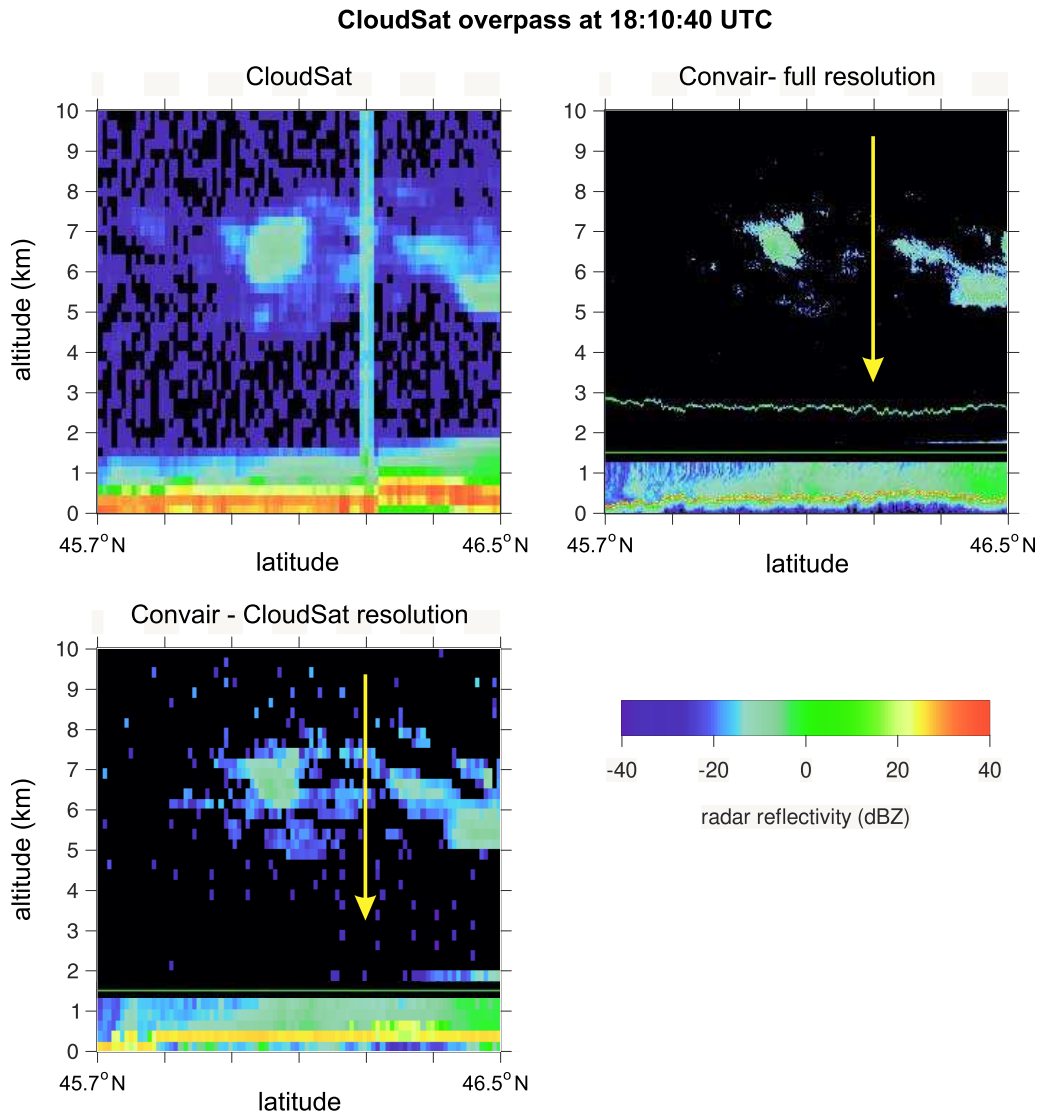


**Figure 8.** (top left) The cross section of CloudSat’s CPR reflectivity measured at 1810:40 UTC on 20 February 2007. The column is a result of detecting the surface reflection of the Convair’s down-facing W-band CPR. The high reflectivity in the column at about 1.5 km is likely the Convair itself. (top right) The cross section of the Convair’s Ka-band radar at 1 s ( $\sim 100$  m) resolution on leg 5 (see Figure 4b). Latitude is indicated along the base of all cross sections and for the Convair corresponds to 916 s of flight. Note the 500 m wide CPR dead zone around the Convair (indicated by green line). Yellow arrow indicates CloudSat overpass. The Convair began flying just below cloud top at the south end of the leg. Note, however, that cloud emerges from the CPR dead zone near the north end. By the end of this leg, cloud top was  $\sim 300$  m above the level flight line. (bottom left) The same as Figure 8 (top right) except Convair reflectivities were averaged up to CloudSat resolution.

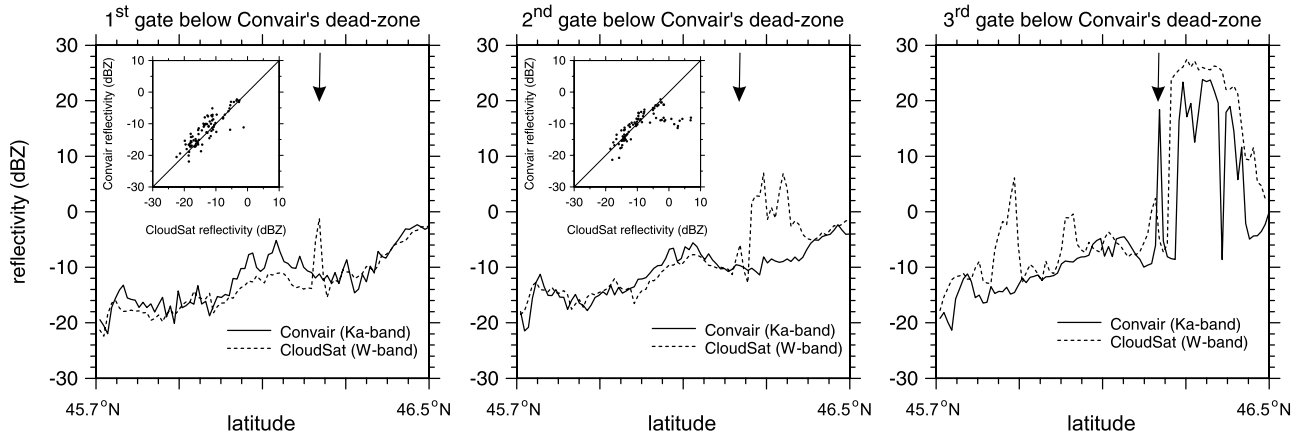


**Figure 9.** Time series, presented as latitude, of radar reflectivities for the first three gates beneath the Convair's CPR dead zone. Convair reflectivities were averaged to CloudSat resolution (see Figure 8). Arrows indicate CloudSat overpass. Receipt by CloudSat of the surface reflection of the Convair's down-facing W-band CPR is evident as a spike in all three plots. Inset scatterplots show the two sets of reflectivities plotted against each other. When the interference spike is removed from the first gate the correlation coefficient is 0.82.

the cross sections through two distinct streams of upper cloud.

[31] Figure 9 shows time series of radar reflectivities for the first three CloudSat gates beneath the Convair's dead zone along with Convair Ka-band reflectivities (averaged to CloudSat resolution). These correspond to distances beneath the Convair of  $\sim 250$  m to  $\sim 1$  km. While it is clear that the radars were observing and responding similarly to the same cloud, the inset scatterplots indicate that Ka-band reflectivities are typically 1 to 2 dB greater than CloudSat's W-band reflectivities (discounting radar interference and surface contamination). Differences of this magnitude are, however, within calibration uncertainties of both radars (see section 3.2.2 and *Im et al.* [2008]). Even the positions and magnitudes of surface noise in the third gate agree well. The fact that CloudSat's radar registers surface noise in the second gate below the dead zone but the Convair's does not can be explained by CloudSat's use of a  $3.3\text{-}\mu\text{s}$  pulse length compared to the Convair's  $1\text{ }\mu\text{s}$ .

[32] Define the second-order structure function for a variable  $\varphi$  as

$$S_2(\psi) = \left\langle [\varphi(t + \psi) - \varphi(t)]^2 \right\rangle \quad (10)$$

where  $t$  is time,  $\psi$  is a time lag, and angular brackets represent mean value.  $S_2(\psi)$  is related, by the Wiener-Khinchine theorem, to the power spectrum [see *Marshak and Davis*, 2005], and is a very intuitive measure of typical fluctuations over a wide range of time (or space). For ranges of  $\psi$  that behave like

$$S_2(\psi) \sim \psi^{\zeta(2)}, \quad (11)$$

$$1 < \beta = \zeta(2) + 1 < 3$$

where  $\beta$  is the spectral exponent of the power spectrum. Figure 10 shows  $S_2(\psi)$  for the series of reflectivities one gate below the Convair's dead zone. While the scaling exponents  $\zeta(2)$  for the two series are very similar, implying that the rate at which fluctuations change with scale are essentially the same for both instruments, the magnitude of CloudSat's fluctuations are systematically smaller than those for the Convair's Ka-band radar. This is visually discernible from both Figures 8 and 9 and probably arises from CloudSat's overlapping of pixels along track. Similarly, Figure 11 shows time series for gates at constant altitudes associated with the upper cloud. In both instances CloudSat and Convair track each other nicely with very respectable agreement in magnitude, though again it is obvious that CloudSat's signals are smoother than the Convair's.

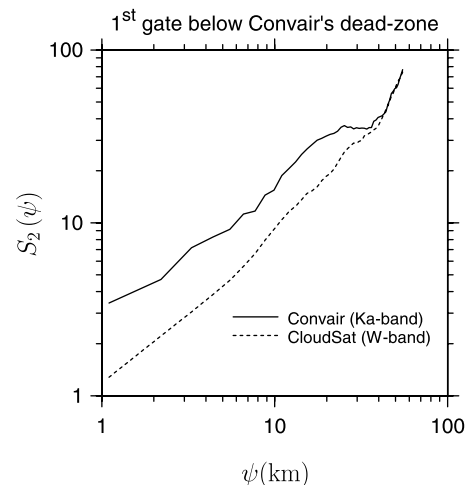


**Figure 10.** Second-order structure functions as functions of horizontal separation for the first CloudSat gate below the Convair's CPR dead zone (see Figures 8 and 9).

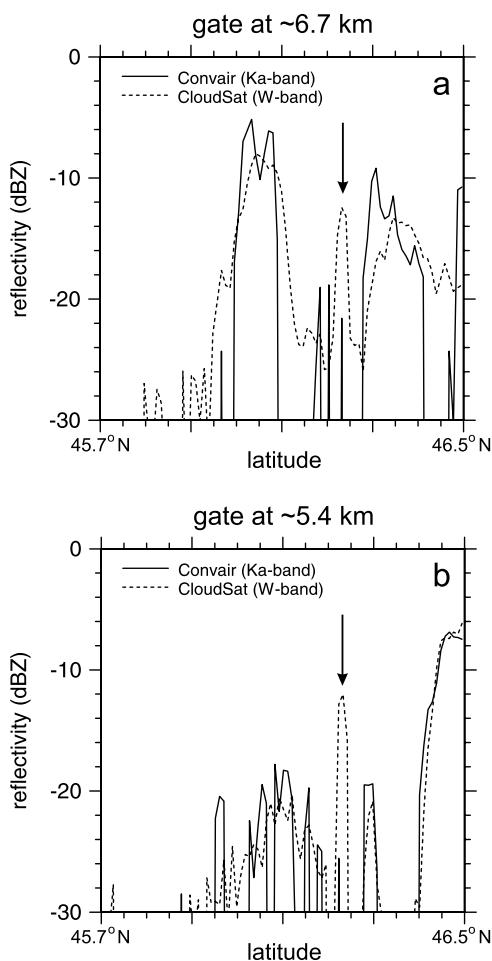


**Figure 11.** As in Figure 9 but these are for two altitudes through the upper cloud (see Figure 8). Again, the Convair's surface-reflected W-band signals are evident as spikes in the CloudSat traces.

#### 4.2. Boundary Layer, Mixed Phase Cloud

[33] Figure 12 shows liquid and ice water contents as well as corresponding droplet and crystal effective sizes inferred by CloudSat algorithms. Shortly before, during, and shortly after CloudSat overpass, the Convair was flying just beneath the top of the boundary layer cloud at an almost constant altitude of  $\sim 1.6$  km above mean sea level. Thus, for the time being, consider only the low cloud deck shown in Figure 12.

[34] Figure 13a shows time series of LWC and IWC on legs 4 and 5 along with Convair altitude. Note that the left side of the plot is southbound and the right northbound. At an altitude of 1.6 km it is clear that LWC increases to the south, but the fact that the Convair had to travel approximately 300 m up to cloud top at the north end (at 1829 UTC) coupled with the slow emergence of cloud above the radar's dead zone (see Figure 8) and the fairly steady decline in LWC to the north suggests the possibility that the cloud was slanted and roughly followed the terrain which rises gently northward. If so, the level flight was effectively a partial vertical sounding of this cloud layer. Figure 13b shows the profile through the uppermost 300 m of cloud at the north

end of the target segment as the plane spiralled up rapidly. It bears the characteristic linear trend in LWC with height associated with mixed adiabatic clouds and resembles closely both the trend shown in Figure 13a from 1806 to 1818 UTC, which is also shown as the scatter of points in Figure 13b, as well as the porpoising profiles between 1745 and 1754 UTC. Figure 13b indicates that while CloudSat's retrievals show, if anything, a slight decrease in LWC with altitude, Figure 12 also shows a steady increase in cloud top altitude from south to north in agreement with Convair data. It also reiterates that CloudSat's horizontal average LWCs over the domain shown in Figures 8 and 12 decrease with height and are actually fairly good coarse-grain estimates. It should be noted that for this cloud segment, typical uncertainties for CloudSat inferred LWC are  $\sim 0.05$  g m $^{-3}$  or about 40% of the inferred values.

[35] Figure 14a shows droplet effective radii along legs 4 and 5 while Figure 14b shows the profile at the north end along with values measured on the northern half of leg 5 and CloudSat's domain average values. CloudSat's values along the majority of the transect are near  $9$   $\mu$ m (see Figure 12), with reported uncertainties of typically  $\sim 1$   $\mu$ m, which are too large by a factor of roughly two. Similarly, though not shown, CloudSat's estimates of droplet concentration are too small; they are typically  $40$  cm $^{-3}$  with an uncertainty of  $\sim 20$  cm $^{-3}$  while Convair values are typically  $300 \pm 100$  cm $^{-3}$ . Clearly, CloudSat's a priori estimation (see section 2.2) lead to, in this case, too few large drops while still accounting for measured CPR reflectivity. Had its retrieval been constrained by additional data, such as MODIS shortwave radiances, it would have almost certainly found a more suitable solution with smaller droplets.

[36] Though not readily observable from Figure 12, CloudSat's estimates of IWC in the low cloud are very small and typically  $\leq 0.002$  g m $^{-3}$ . While the enhancement near the middle of the transect, as seen in Figure 12, is mildly discernible in CloudSat data, they are still much smaller than Nevzorov values that hover between 0.01 and 0.1 g m $^{-3}$ . So while CloudSat identified, correctly, a mixed phase low cloud, the amount of ice it inferred was an order of magnitude too small. Again, had its routine opted for more ice, which would still have almost inconsequential impacts on cloud optical properties at visible wavelengths, that would have lead to a prediction of more smaller droplets.

[37] Figure 15a shows that for the low cloud, the lion's share of extinction is due to liquid droplets with  $\kappa$  reaching  $100$  km $^{-1}$  in the south, consistent with many small droplets, leveling off to  $\sim 30$  km $^{-1}$  near overpass, and falling to  $10$  km $^{-1}$  in the north. Figure 15b shows values for the last half of leg 5, the rapid climb at 1829 UTC, and CloudSat's domain averages assuming  $Q_{\text{ext}} = 2$ . The upshot is that CloudSat's radar-only retrieval underestimates total optical depth  $\tau$  of the low cloud. Generally, CloudSat designated cloud to be only  $\sim 250$  m thick, with mean extinction of  $\sim 15$  km $^{-1}$ , and thus  $\tau \simeq 4$ . Using the profile of extinction observed on the climb at 1829 UTC, the Convair's estimate of  $\tau$  is  $\sim 8$ .

#### 4.3. Cirrus Ice Cloud

[38] As shown already in Figure 8, when the Convair's Ka-band reflectivities are reduced to CloudSat resolution

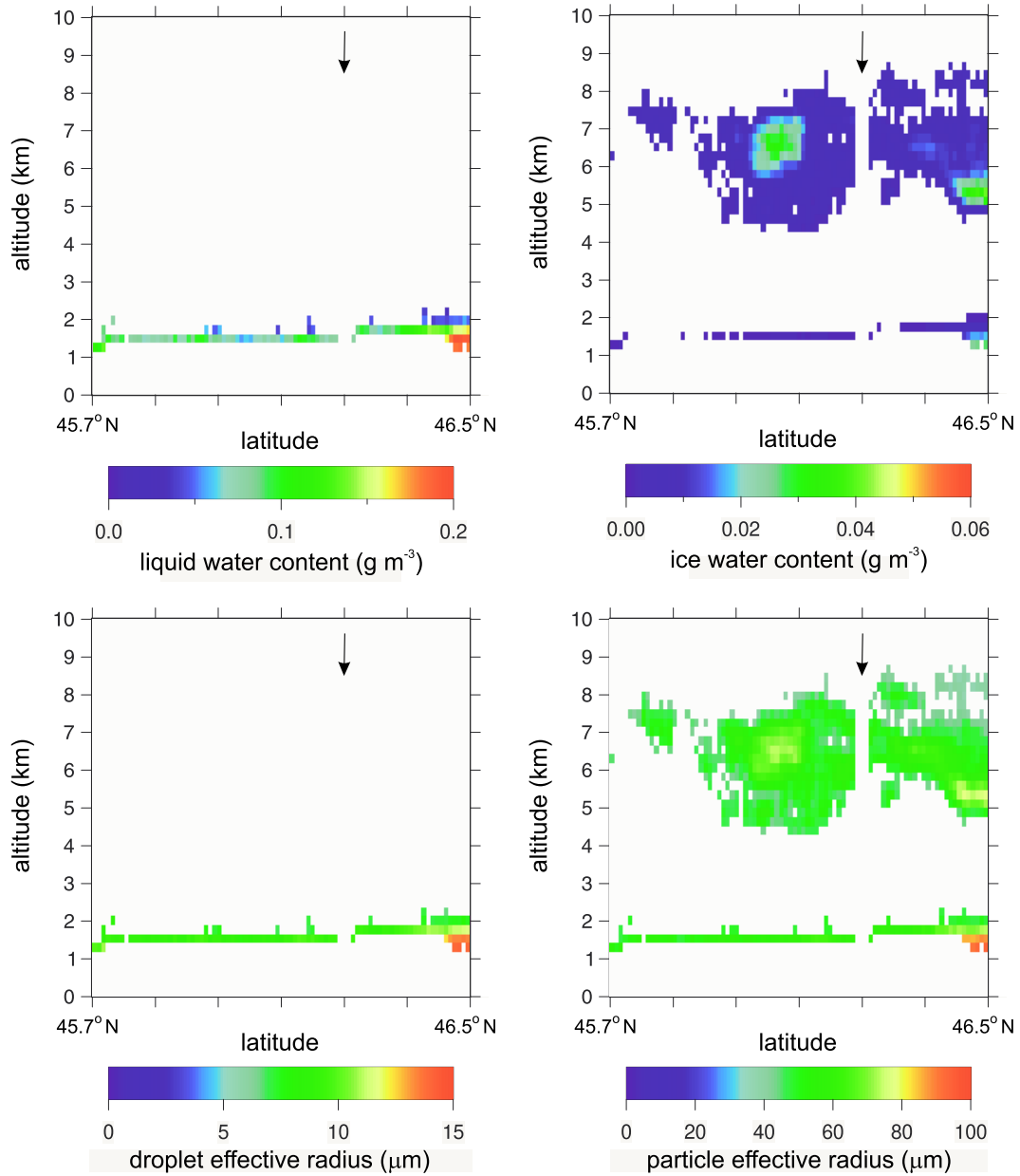


**Figure 12.** Cross sections of liquid and ice water contents and corresponding cloud particle effective radii inferred from CloudSat CPR reflectivities. The arrows indicate overpass with the Convair (note the associated blank column).

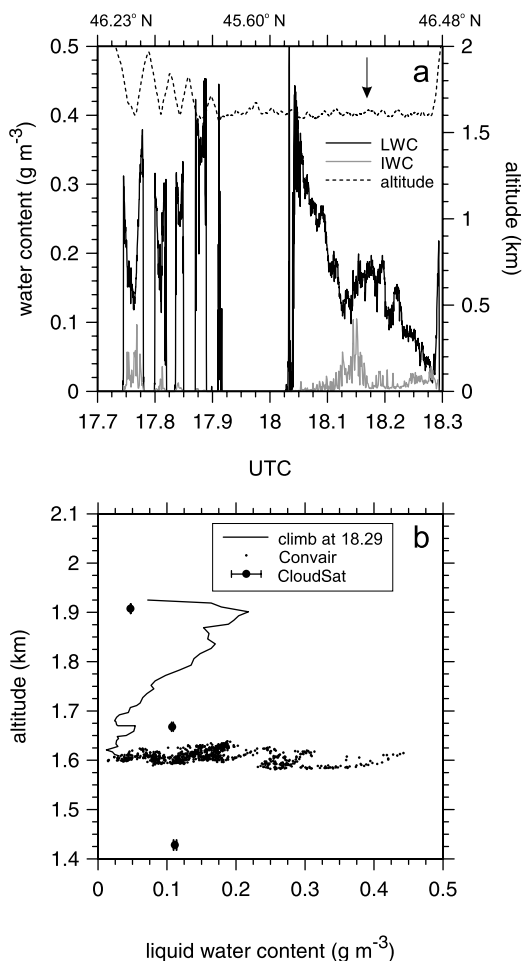


**Figure 13.** (a) Cloud liquid (LWC) and ice (IWC) water contents as measured on the Convair as functions of time (latitude listed on top). Corresponding Convair altitude is also shown. The southbound leg 4 is on the left, and the northbound leg 5 is on the right. Arrow indicates CloudSat overpass. (b) Line represents cloud LWC as a function of altitude measured by Convair during its ascent at the termination of leg 5 (extreme right of plot in Figure 13a). Dots are Convair values measured along the level portion of leg 5. Solid circles are mean values inferred from CloudSat reflectivities, and error bars indicate standard deviation across the 60 nautical mile segment.

they agree well with CloudSat's reflectivities for the high cloud. Consider now some of the properties of the high cloud obtained through in situ sampling by the Convair and how they compare, despite not being contemporaneous, to inferences drawn from CloudSat data.

[39] Figure 4 shows that legs 1 and 6 were flown above 5 km and hence the Convair was often in situ with respect to the upper cloud. Analysis of 2-D imagery of ice crystals was performed on data produced by the 2DC and 2DP probes. Figure 16 shows that typically 80% to 90% of the crystals were classifiable as irregular. Spheres, needles, and dendrites generally accounted for the remaining  $\sim 15\%$ ; but very occasionally comprised up to  $\sim 50\%$  thereby forming pockets with high concentrations of needles or quasi-spherical ice

particles identified as spheres. Following the definition used by Korolev and Sussman's [2000] algorithm, irregular particles were defined as particles not classified as dendrites, spheres, or needles/columns. Visual analysis of the images indicated that most ice particles along legs 1 and 6 can be identified as bullet rosettes. Also from the 2-D probes, and Figure 16, it can be seen that IWC averaged over 4 s of flight (or  $\sim 400$  m) ranged from 0.01 to  $0.02 \text{ g m}^{-3}$ ; yet peaked near  $0.09 \text{ g m}^{-3}$ . Figure 12 shows that CloudSat inferred IWCs, at significantly reduced vertical and horizontal resolution, resemble Convair values fairly well; especially given that CloudSat reported uncertainties are typically near 40% and that data were acquired at different times. This is better seen in Figure 17 which shows frequency distributions of IWC for legs 1 and 6 for the Convair and for the entire upper cloud detected by CloudSat (between 4.5 km and 9 km). Both distributions can be approximated well by gamma functions, and the fact that their slopes resemble one another indicates that their coefficients of variation are similar too.

[40] It is difficult to reconcile measured and inferred crystal sizes so inferred concentrations and approximate extinctions are compared instead. Figure 16 shows that for

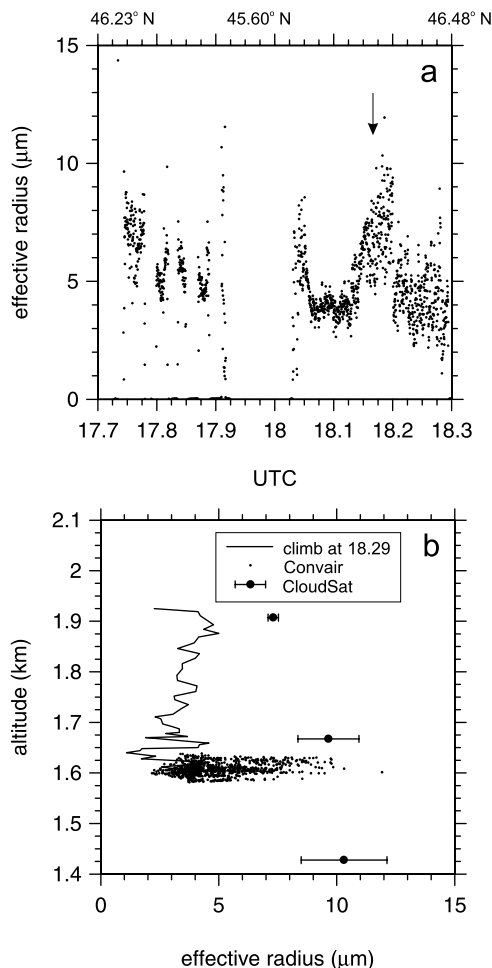


**Figure 14.** As in Figure 13 except this is for droplet effective radius. Error bars on CloudSat values indicate standard deviation across the 60 nautical mile segment.

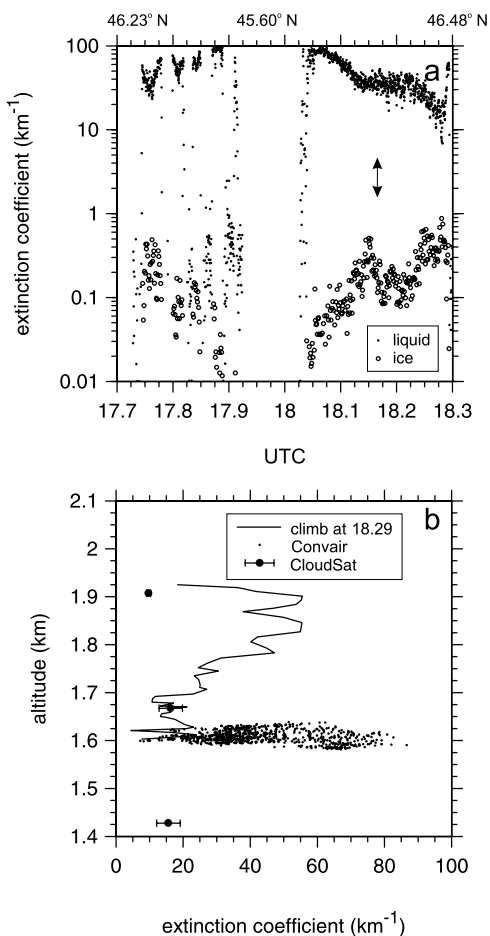


**Figure 15.** (a) Dots represent liquid-phase cloud extinction coefficient as a function of time (latitude listed on top). Open circles are corresponding ice-phase values. Arrow indicates CloudSat overpass. (b) Line represents cloud extinction coefficient for liquid-phase clouds. Also, the scatter of points is only over the second half of leg 5.

the upper cloud the Convair’s probes detected typically 3 to 10 crystals per liter of air but jumped as high as  $25 \text{ l}^{-1}$ . In contrast, Figure 18a shows that for this segment CloudSat’s estimates, at lower spatial resolution, were rarely less than  $10 \text{ l}^{-1}$ , as high as  $51 \text{ l}^{-1}$ , yet characterized by uncertainties of 50%. Given the relatively good agreement for IWC distributions, it is consistent that Convair crystal radii were typically 100 to 200  $\mu\text{m}$  while CloudSat’s inferences were typically 50  $\mu\text{m}$ . Differences this large indicate poor agreement regardless of how one defines effective size, and uncertainty, of crystals. Note that CloudSat’s prior estimates went in opposite directions for high and low cloud; while it inferred too few small particles for the largely liquid-phase low cloud, it satisfied CPR reflectivities for the high cloud by predicting too many small particles.

[41] Finally, Figure 16 shows crystal extinction coefficient both measured directly with the extinction probe (1 s data) and calculated using 2-D probe data (4 s data). Agreement is acceptable given that calculating  $\kappa$  makes many assumptions about the dependence of extinction on particle size and shape. These calculations were suited best

to irregular crystals which largely explains the general agreement. Moreover, the relative abundance of high and low spikes in the extinction probe trace is due to higher resolution; which had to be degraded for the 2-D probes in order to obtain meaningful statistics. At any rate, Convair values are typically between 0.2 and  $1 \text{ km}^{-1}$ . Figure 18b shows that CloudSat’s estimates of  $\kappa$  for ice cloud, assuming again that  $Q_{\text{ext}} \simeq 2.0$ , range primarily between 0.1 and  $0.8 \text{ km}^{-1}$  implying very good agreement with in situ measurements.

## 5. Discussion and Conclusions

[42] The objective of NASA’s pioneering CloudSat mission is simply to improve the representation of clouds in GCMs by providing the first global view of vertical and horizontal microstructural and macrostructural characteristics of clouds. The activity of satellite remote sensing has many facets beginning with development of mathematical inversion methods, often directed by a science plan, which moves on to a mission design programme, and, in a sense, ends with application of inferred products that give rise to knowledge and new hypotheses that feedback to produce new inversion techniques and new science plans. One distinct facet of this cascading feedback process is post-launch assessment of retrieved products. These activities are characterized generally by dedicated campaigns that gather independent data that are commensurate with retrieved products. When a mission’s scope is global, as CloudSat’s is, it should have multiple assessment campaigns that target a diversity of atmospheric-surface conditions. This has been so with CloudSat, and one such campaign was the Canadian CloudSat-CALIPSO Validation Project (C3VP) which took place in southern Canada during winter 2006/2007.

[43] C3VP’s primary objective is assessment of CloudSat retrieved cloud and precipitation properties for cold weather conditions. The airborne component of C3VP consisted of flying the NRC Convair-580, a research aircraft chock full of NRC and Environment Canada cloud monitoring instruments, beneath the overpassing CloudSat satellite. Twenty-one flights were conducted both inside and outside of clouds. This report focused on the flight that took place over southern Quebec on 20 February 2007. Clouds during this flight were multilayer and mixed phase with radar reflectivities that were often near the lower detection limit of CloudSat’s radar.

[44] For the most part, CloudSat’s W-band and the Convair’s Ka-band radar reflectivities agree extremely well with differences typically less than  $\pm 3 \text{ dB}$  and rarely exceeding 5 dB (discounting ground contamination). While this was not surprising given that the cloud particles encountered on that flight were generally small relative to radar wavelengths, it provides confirmation that both radar systems were very likely functioning as intended.

[45] One of the largest challenges for CloudSat, and all remote sensing activities, involves mixed phase clouds. The manner in which this is presently handled by CloudSat was discussed briefly in section 2.2. The upshot is that for cells in a column with  $-20^\circ < T < 0^\circ$ , CloudSat is likely to report, by default, mixed phase clouds. How often this translates into positive and negative predictions of mixed phase cloud, and their respective properties when positive,

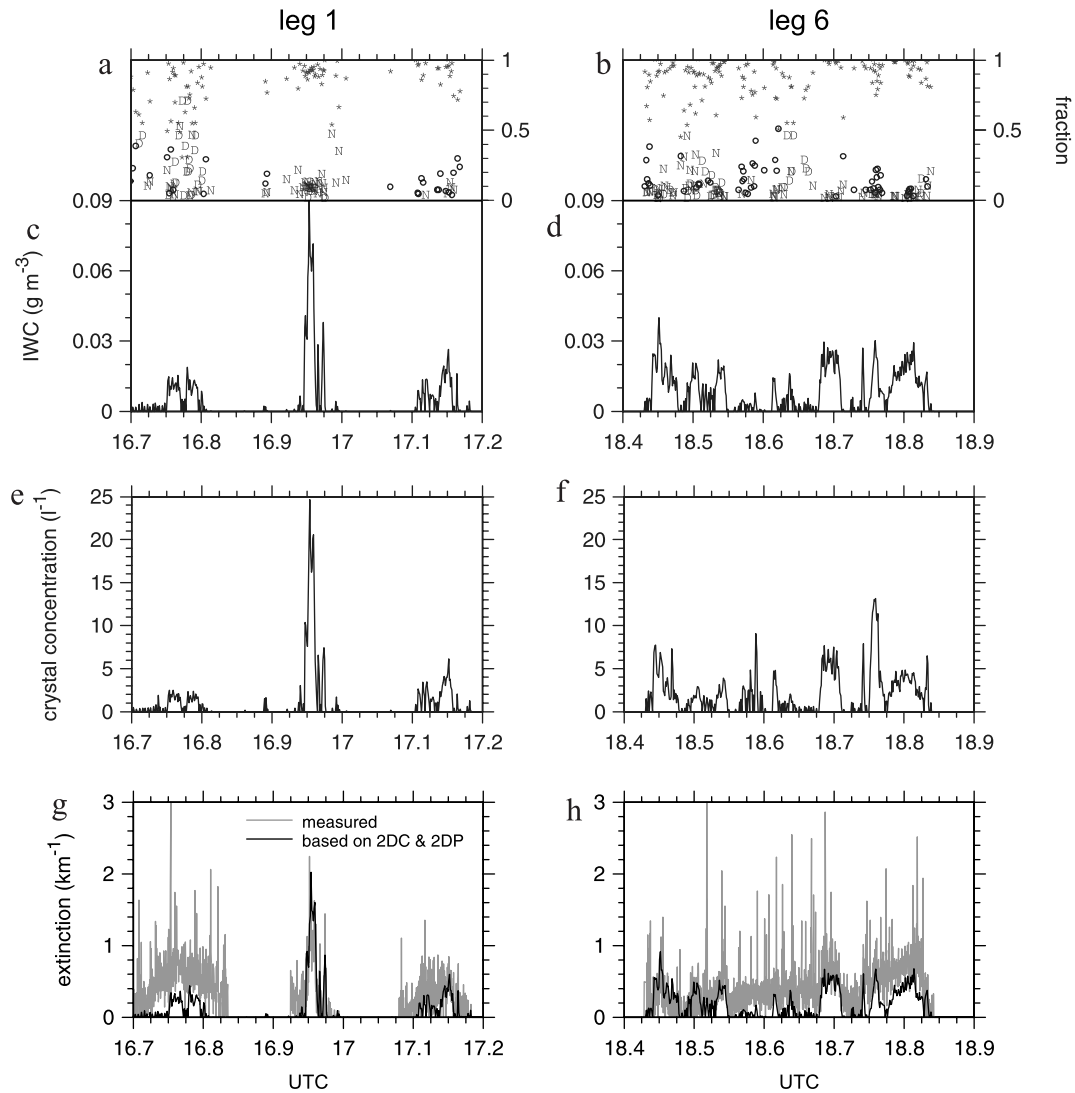


**Figure 16.** (a and b) Fractional number of crystals as a function of time for the high cloud sampled on legs 1 and 6 (see Figure 4). Crystals were identified using image recognition software and OAP 2-D optical probe imagery. Asterisks represent irregulars, circles are for spheres, D is for dendrites, and N is for needles. Corresponding values of (c and d) ice water content (IWC), (e and f) crystal concentration, and (g and h) extinction coefficient. All quantities were derived from 2-D probe imagery and correspond to 4 s integrations save for the measured extinction coefficient which came from the extinction probe integrated for 1 s.

remains to be seen. Nevertheless, it is not a guarantee that ice and liquid will be reported for all cells with  $-20 < T < 0^\circ$ . Figure 12 showed that ice was not reported in several cells of the low cloud despite ECMWF reporting  $T \simeq -7^\circ\text{C}$ . The upper cloud was unambiguous as its highest reported temperature was  $-22^\circ\text{C}$  and indeed the Convair sensed no liquid.

[46] For the cloud studied here it is clear that CloudSat's assumptions lead to low cloud extinction being underestimated by 50% in conjunction with an overestimate of droplet effective radius coupled with a less severe underestimate of water content. CloudSat's optimal estimation inversion does not permit, as yet, large numbers of very small droplets. If the inversion process were constrained by MODIS shortwave radiances in addition to just radar reflectivities, there is little doubt that the quality of the estimates would improve.

[47] On the whole, CloudSat retrieval of the upper cloud's extinction coefficient performed well. Ice water content estimates were on the low side but the form of the frequency distribution was captured well. Crystal concentrations were at least twice as large as those reported by the Convair's 2-D probes and hence effective sizes of crystals appear to be too small by a factor of  $\sim 2$  (which coupled with the underestimated water content lead to reasonably good estimates of extinction).

[48] In many respects a project like C3VP is difficult to both execute and draw sound conclusions from given the resources at hand. The sampling volume of an instrument on a single aircraft is actually very small relative to the coarse cross-sectional data of CloudSat, and so intercomparison is inherently inexact and often fraught with uncertainty and difficulty. Nevertheless, it is difficult to overstate the importance, and luxury, of having in situ samples of the very characteristics that one is attempting to infer remotely. The results presented here demonstrate that upon scrutiny, CloudSat is performing as well as, if not much better than, expected; recognizing that this initial round of products are

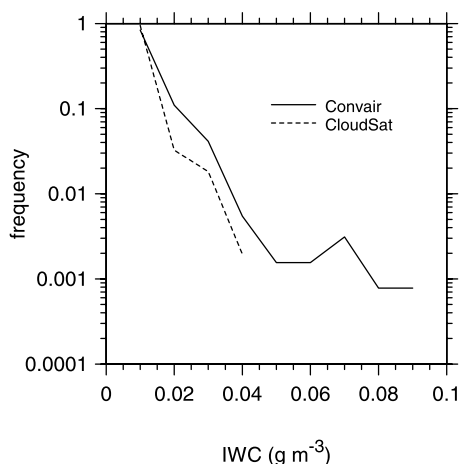


**Figure 17.** Frequency distributions of cloud ice water contents for the two Convair series shown in Figure 11 and for the entire upper cloud as seen by CloudSat (see Figure 12).

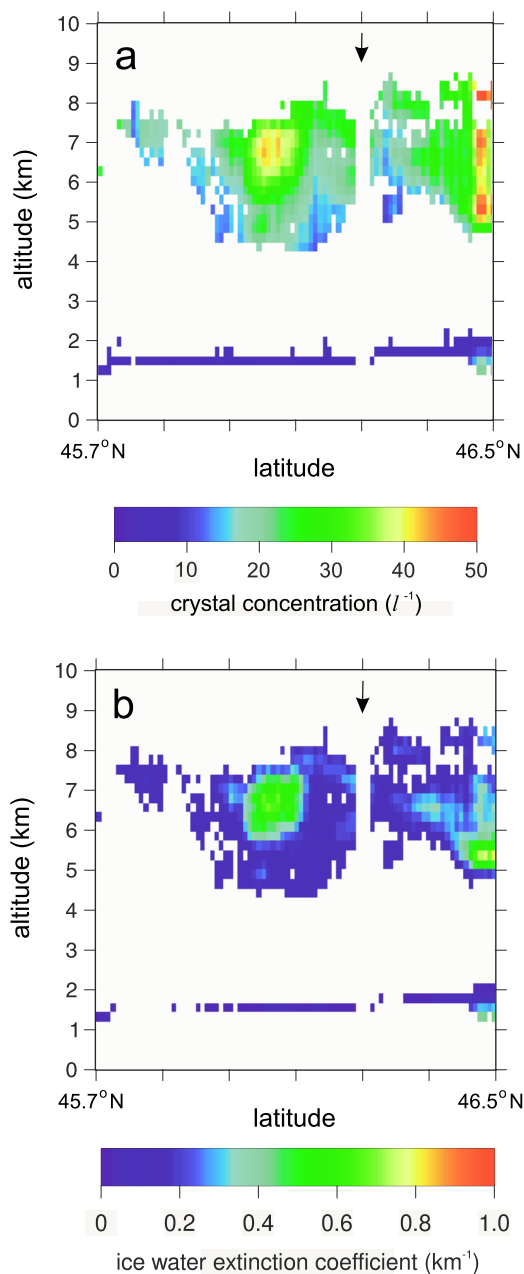


**Figure 18.** (a) Ice crystal concentration as inferred by CloudSat CPR reflectivities. Arrow and coincident blank column indicate overpass with the Convair. (b) As in Figure 18a except this is for approximate extinction coefficient for ice-phase cloud. Note that crystal extinction efficiency was assumed to be 2.

radar only. Once CloudSat data synergize with data from other A-train satellites one can only expect the quality of retrievals to improve over those assessed here.

[49] **Acknowledgments.** C3VP was made possible by funds provided by the Canadian Space Agency (CSA) and by in-kind support from the National Research Council (NRC) of Canada and Environment Canada (EC). We are specially indebted to Stella Mello and Thomas Piekutowski of the CSA, Peter Rodriguez (EC) for help with Convair radar data, Rob Reed (EC) for instrument maintenance, and the NRC pilots who expertly, and routinely, contaminated CloudSat data with the Convair-580.

## References

- Austin, R. (2007), Level 2B radar-only cloud water content (2B-CWC-RO) process description document, CloudSat Data Processing Cent., Coop. Inst. for Res. in the Atmos., Colo. State Univ., Fort Collins. (Available at <http://cloudsat.cira.colostate.edu/dataICDlist.php?go=list&path=/2B-CWC>)
- Barker, H. W. (2008), Representing cloud overlap with an effective decorrelation length: A radiative assessment using CloudSat and CALIPSO data, *J. Geophys. Res.*, doi:10.1029/2008JD010391, in press.
- Barker, H. W., J. N. S. Cole, J.-J. Morcrette, R. Pincus, P. Räisänen, K. von Salzen, and P. A. Vaillancourt (2008), The Monte Carlo independent column approximation: An assessment using several global atmospheric models, *Q. J. R. Meteorol. Soc.*, *134*, 1463–1478.
- Baumgardner, D., J. W. Strapp, and J. E. Dye (1985), Evaluation of the forward scattering spectrometer probe. Part II: Corrections for coincidence and dead-time losses, *J. Atmos. Oceanic Technol.*, *2*, 626–632.
- Brown, P. R. A., and P. N. Francis (1995), Improved measurements of the ice water content in cirrus using a total-water probe, *J. Atmos. Oceanic Technol.*, *12*, 410–414.
- Fox, N. I., and A. J. Illingworth (1997), The retrieval of stratocumulus cloud properties by ground-based cloud radar, *J. Appl. Meteorol.*, *36*, 485–492.
- Hudak, D. R., H. W. Barker, P. Rodriguez, and D. P. Donovan (2006), The Canadian CloudSat Validation Project, paper presented at 4th European Conference on Radar in Hydrology and Meteorology, Serv. Meteorol. de Catalunya, Barcelona, Spain.
- Illingworth, A. J., et al. (2007), Cloudnet, *Bull. Am. Meteorol. Soc.*, *88*, 883–898.
- Im, E., S. Tanelli, S. L. Durden, and K. Pak (2008), Cloud profiling radar performance, paper presented at International Geoscience and Remote Sensing Symposium, Inst. of Electr. and Electron. Eng., Barcelona, Spain.
- Jordan, J. E., J. W. Strapp, D. R. Hudak, P. Rodriguez, K. B. Strawbridge, and L. E. Lillie (2000), First results from the Canadian Convair (NRC) 35 GHz cloud-profiling radar during AIRS, paper presented at Geoscience and Remote Sensing Society Conference, Inst. of Electr. and Electron. Eng., Honolulu, Hawaii, 24–28 July.
- King, W. D., D. A. Parkin, and R. J. Handsworth (1978), A hot-wire water device having fully calculable response characteristics, *J. Appl. Meteorol.*, *17*, 1809–1813.
- Knollenberg, R. G. (1981), Techniques for probing cloud microstructure, in *Clouds, Their Formation, Optical Properties, and Effects*, edited by P. V. Hobbs and A. Deepak, pp. 15–89, Academic, New York.
- Korolev, A. V., and B. Sussman (2000), A technique for habit classification of cloud particles, *J. Atmos. Oceanic Technol.*, *17*, 1048–1057.
- Korolev, A. V., J. W. Strapp, G. A. Isaac, and A. N. Nevzorov (1998), The Nevzorov airborne hot-wire LWC-TWC probe: Principle of operation and performance characteristics, *J. Atmos. Oceanic Technol.*, *15*, 1495–1510.
- Korolev, A. V., G. A. Isaac, S. G. Cober, J. W. Strapp, and J. Hallett (2003), Microphysical characterization of mixed-phase clouds, *Q. J. R. Meteorol. Soc.*, *129*, 39–66.
- Korolev, A., J. W. Strapp, G. Isaac, and E. Emery (2008), Improved airborne hot-wire measurements of ice water content in clouds, paper presented at International Conference on Clouds and Precipitation, Cen. de Cienc. de la Atmos., Univ. Nac. Auton. de Mex., Cancun, Mex., July.
- L'Ecuyer, T. S., and G. L. Stephens (2002), An estimation based precipitation retrieval algorithm for attenuating radars, *J. Appl. Meteorol.*, *41*, 272–285.
- Marshak, A., and A. B. Davis (2005), Scale-by-scale analysis and fractal cloud models, in *3D Radiative Transfer in Cloudy Atmospheres*, edited by A. Marshak and A. B. Davis, pp. 654–664, Springer, Heidelberg, Germany.
- Sekelsky, S. M., W. L. Ecklund, J. M. Firda, K. S. Gage, and R. E. McIntosh (1999), Particle size estimation in ice-phase clouds using multifrequency radar reflectivity measurements at 95, 33, and 2.8 GHz, *J. Appl. Meteorol.*, *38*, 5–28.
- Slingo, A., and J. M. Slingo (1991), Response of the National Center for Atmospheric Research community climate model to improvements in the representation of clouds, *J. Geophys. Res.*, *96*, 15,341–15,357.
- Stephens, G. L., et al. (2002), The CloudSat mission and the A-Train, *Bull. Am. Meteorol. Soc.*, *83*, 1771–1790.
- Stevens, B., G. Vali, K. Comstock, R. Wood, M. C. Van Zanten, P. H. Austin, C. S. Bretherton, and D. H. Lenschow (2005), Pockets of open cells and drizzle in marine stratocumulus, *Bull. Am. Meteorol. Soc.*, *86*, 51–57.
- Strawbridge, K. B., and B. J. Snyder (2004), Daytime and nighttime aircraft lidar measurements showing evidence of particulate matter transport into the northeastern valleys of the Lower Fraser Valley, B.C., *Atmos. Environ.*, *38*, 5873–5886.
- Twohy, C. H., A. J. Schanot, and W. A. Cooper (1997), Measurement of condensed water content in liquid and ice clouds using an airborne counterflow virtual impactor, *J. Atmos. Oceanic Technol.*, *14*, 197–202.
- Verlinde, J., et al. (2007), The Mixed-Phase Arctic Cloud Experiment, *Bull. Am. Meteorol. Soc.*, *88*, 205–221.
- Wiscombe, W. J. (1980), Improved Mie scattering algorithms, *Appl. Opt.*, *19*, 1505–1509.
- H. W. Barker, D. R. Hudak, A. V. Korolev, and J. W. Strapp, Cloud Physics and Severe Weather Research Section, Environment Canada, Toronto, ON M3H 5T4, Canada. (howard.barker@ec.gc.ca)
- K. B. Strawbridge, Centre for Atmospheric Research Experiments, Environment Canada, RR#1, 6248 Eighth Line, Egbert, ON L0L 1N0, Canada.
- M. Wolde, Institute for Aerospace Research, National Research Council of Canada, U-61, 1200 Montreal Road, Ottawa, ON K1A 0R6, Canada.